Holmi, Joonas T.; Raju, Ramesh; Ylönen, Jonas; Subramaniyam, Nagarajan; Lipsanen, Harri

# Optical amplification by surface-plasmon-resonant Au grating substrates: Monolayer MoS2 with 170-fold second harmonic generation and 3-fold (off-resonance) Raman scattering

*Published in:*
Superlattices and Microstructures

*DOI:*
10.1016/j.spmi.2021.107077

Published: 01/12/2021

*Document Version*
Publisher's PDF, also known as Version of record

Holmi, Joonas T.; Raju, Ramesh; Ylönen, Jonas; Subramaniyam, Nagarajan; Lipsanen, Harri

# Optical amplification by surface-plasmon-resonant Au grating substrates: Monolayer MoS2 with 170-fold second harmonic generation and 3-fold (off-resonance) Raman scattering

*Published in:*
Superlattices and Microstructures

*DOI:*
10.1016/j.spmi.2021.107077

Published: 01/12/2021

*Document Version*
Publisher's PDF, also known as Version of record

Superlattices and Microstructures 160 (2021) 107077

Contents lists available at ScienceDirect

Superlattices and Microstructures

journal homepage: www.elsevier.com/locate/superlattices

# Optical amplification by surface-plasmon-resonant Au grating substrates: Monolayer $MoS_2$ with 170-fold second harmonic generation and 3-fold (off-resonance) Raman scattering

Joonas T. Holmi [a,*], Ramesh Raju [a,**], Jonas Ylönen [b], Nagarajan Subramaniyam [b], Harri Lipsanen [a]

[a] Department of Electronics and Nanoengineering, Aalto University, P. O. Box 13500, FI-00076, Finland
[b] Xfold Imaging Oy, Otakaari 5 A, Espoo, FI-02150, Finland

ARTICLE INFO

*Keywords:*
Surface-enhanced light-matter interactions
Amplified nonlinear optical processes
Surface-plasmon-resonance optimized metal gratings
Two-dimensional van der Waals materials for on-chip photonic devices

ABSTRACT

Nanoplasmonics is a potential game-changer in the development of next-generation on-chip photonic devices and computers, owing to the geometrically controlled and amplified linear and nonlinear optical processes. For instance, it resolves the limited light-matter interaction of the unique two-dimensional (2D) crystalline materials like semiconducting monolayer molybdenum disulfide (1L-$MoS_2$). Metal grating (MG) substrates excel at this because their surface plasmons (SPs) can lead to stark field confinement near the surface. This work studies optical amplification of 1L-$MoS_2$ on the gold (Au) MG substrate, which was designed to operate in a glycerol environment with SP resonance (SPR) at 850 nm excitation wavelength. Its design was verified by simulated and experimental reflectances, and topographically inspected by atomic force microscopy (AFM). Two advanced imaging modalities, second harmonic generation (SHG) and confocal Raman microscopy (CRM) were used to evaluate its 170-fold SHG on- and 3-fold CRM off-resonance optical amplifications, respectively. Some $MoS_2$-to-grating adhesion issues due to trapped liquid showed as image nonuniformities. Possible improvements to limitations like surface roughness were also discussed. These Au MG substrates can boost conventional linear and nonlinear backscattering microscopies because they are tunable in the visible and near-infrared range by selecting geometry, metal, and environment.

## 1. Introduction

Nanoscale manipulation and boost of light-matter interaction via plasmonic metal nanostructures have enabled many attractive applications such as miniaturization of photonic devices [1–5], amplification of optical processes (nonlinear [4,6,7], refractive index [8,9], absorbance [6,10]), reduction of light-induced damage [11], and improvement of existing implementations (light-emitting

*Abbreviations:* 1L-$MoS_2$, monolayer molybdenum disulfide; 2D, two-dimensional; AFM, atomic force microscopy; Au, gold; BF, bright field; CRM, confocal Raman microscopy; EBL, electron-beam lithography; MG, metal grating; RMS, root-mean-square; SHG, second harmonic generation; SP, surface plasmon; SPR, surface plasmon resonance; VLS, vapour-liquid-solid.

* Corresponding author.
** Corresponding author.
*E-mail addresses:* jtholmi@gmail.com (J.T. Holmi), ramesh.raju@aalto.fi (R. Raju).

https://doi.org/10.1016/j.spmi.2021.107077
Received 31 August 2021; Received in revised form 12 October 2021; Accepted 21 October 2021
Available online 2 November 2021

diodes [12], biological [8,13,14] and chemical [13,15,16] sensors). Localized optical amplification is enabled by SPs, which are collective oscillations of free electrons in the metal, coupled with the incoming electromagnetic radiation [1]. There are two types of SPs, localized SPs [15] and propagating SP polaritons [4], both of which require specific excitation wavelengths to resonate. Interestingly, in the SPR-active MGs, both have been shown to contribute to the strong field confinement in the vicinity of the metal surface [7,17]. Such plasmonic MGs can be used with conventional microscopes [6,13] to obtain the same optical signal but with much lower laser power, reducing the laser-induced effects like sample damage. They are particularly attractive when applied to nonlinear optical processes like SHG due to the quadratic or higher amplification [4,6,7], which can be used to improve applications such as optical frequency conversion [7,18,19], optical switching [5], and nonlinear spectroscopic detection of chemical fingerprints [4,6,7,13].

The recent rise of 2D crystalline materials, such as graphene, hexagonal boron nitride, and transition metal dichalcogenides, has sparked many new developments in electronics and photonics [20–23]. However, their light-matter interaction can be too limited for practical use due to their subwavelength thickness, which can be remedied by a hybrid structure of 2D materials and MG substrate [3,5,10,19,24–27]. This work studies the hybrid of a semiconducting 1L-$MoS_2$ and an Au MG, which may enable promising optoelectronic devices [3,10,26] like photodetectors [3]. The Au MG substrate was geometrically SPR-optimized to 850 nm excitation wavelength and glycerol environment. A 170-fold on-resonance SHG amplification is reported with some spatial inhomogeneities due to the $MoS_2$-to-grating adhesion issues. The Au MG substrate was also intentionally tested beyond its design in an off-resonance regime using a 532 nm laser and air environment, but it still showed a 3-fold increase in CRM of 1L-$MoS_2$. The design flexibility and fabrication issues like surface roughness were also discussed and improvements were proposed. These MG substrates are particularly useful in biological imaging applications due to the reduced photobleaching and the selective optical amplification, and are already being sold for this purpose [28]. Interestingly, they may even have uses as label-free biosensors based on the recent developments of plasmonic-based viral diagnostics [29,30].

## 2. Fabrication and characterization

The studied 1L-$MoS_2$ was vapour-liquid-solid (VLS) grown in a dual-zone thermal tube furnace [31,32]. Initially, the $SiO_2$/Si substrates were spin-coated with a 5 mg/mL $Na_2MoO_4$ solution. Then, the zone 1 upstream was loaded with 100 mg of sulphur, and the Ar carrier gas flow rate was set to 70 sccm. To begin, the zone 1 and 2 temperatures were simultaneously heated up to 200 °C at 2.3 °C/min (for sulphur evaporation) and 800 °C at a rate of 10 °C/min (for $Na_2MoO_4$ evaporation and $MoS_2$ growth), respectively. Then, their temperatures were kept constant for 5 min, during which triangular $MoS_2$ flakes with S-terminal zigzag edges [33] started to form at the sulphur-$Na_2MoO_4$ mixture droplets. Finally, the substrate was allowed to cool down naturally to room temperature. The prepared 1L-$MoS_2$ was transferred to the patterned Au/Si-substrate manufactured and patented [34] by Xfold Imaging Oy. The Au MG substrate was fabricated using electron-beam lithography (EBL) and evaporation techniques. Its SPR was geometrically optimized for 850 nm plane wave excitation and glycerol solution, which was observed as a resonance dip in the unpolarized reflectance measurements.

The fabricated samples were characterized by two advanced imaging techniques, SHG and CRM. The focused laser beam width was about 1 μm in all cases. The SHG scans were done with Leica TCS SP8 CARS microscope using a 25×/0.95 water-immersion objective lens and a tunable 800–920 nm picosecond laser (APE PicoEmerald) at 0.7–1.0 W power (5–6 ps pulse duration and 80 MHz repetition rate). The CRM scans were performed with WITec alpha300 RA+ microscope using a 20×/0.40 dry objective lens and a 532 nm

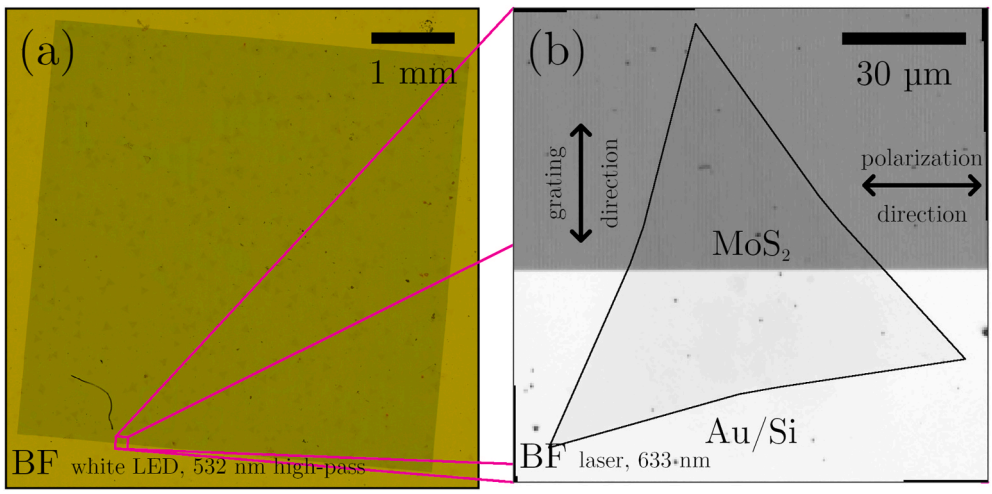


**Fig. 1.** The BF images of the triangular 1L-$MoS_2$ flakes transferred on the Au MG substrate. Image (a) shows the 5 × 5 mm SPR-active grating area, where a 1L-$MoS_2$ flake marked on the bottom-right was ideal for the resonance test due to its location on the grating edge. Image (b) zooms in to this flake with 9–10° clockwise rotation and depicts its 633 nm laser-scanned BF response. The incident light polarizations were always perpendicular to the grating groove direction to excite the SPR-active area.

continuous-wave laser at 6 mW power. In addition, the bright field (BF) images were taken with Leica by a HeNe 633 nm laser. The unpolarized reflectance response for another Au MG substrate of the same batch was obtained under similar measurement conditions using a custom-built setup. Finally, the topographic images were taken with the Bruker Dimension Icon system by AFM in peak-force tapping mode. All data analysis, lossless image-to-image alignment and downscaling, and other post-processing steps were done by MATLAB software and MATLAB data evaluation toolbox, WITio v2.0.0 [35] (for the WITec microscope datasets).

## 3. Surface topography and optical amplification

The optical amplification of 1L-$MoS_2$ and the grating surface morphology that enables it are presented and discussed in the remainder of the paper. The studied VLS-grown 1L-$MoS_2$ transferred on the 850-nm/glycerol-optimized Au MG substrate were mostly three-point stars as is optically shown in Fig. 1a,b. About 6% of the 5 × 5 mm Au grating area was covered with 1L-$MoS_2$ flakes. One particularly interesting flake in Fig. 1b was found to overlap the grating edge, allowing quick evaluation of the optical amplification. All measurements were performed in only the cross-polarized case because SPs can only be excited by the light polarization perpendicular to the vertical grating direction, which has been shown by previous studies and simulations [10,26].

### 3.1. Surface morphology by AFM scans

The nanoscale topography of the Au MG substrate in the vicinity of the 1L-$MoS_2$ flake is revealed by the AFM scans in Fig. 2a–c. The grating pitch was estimated from the cross-section profile in Fig. 2b and is 486 ± 1 nm on average. The average grating spacing and height are 87 nm and 61 nm, respectively. The grating vertical edges were also slightly sloped at a 26.6 ± 0.8° angle. Some surface granularity is seen in Fig. 2b with 2 nm root-mean-square (RMS) roughness. The quantile-based 95% confidence interval shows that the parameters may vary up to 19 nm in width and 11 nm in depth directions. It is noteworthy that the AFM scan in Fig. 2b also revealed unintentional alternating-pitch, in which the grating spacing remains constant, but the grating pitch is 466 nm for odd lines and 506 nm for even lines. Although the exact cause is unknown, it is expected to be related to the EBL pixel resolution of 20 nm. Another Au MG substrate from the same batch was checked and it had a 488 ± 1 nm pitch on average, but showed no pitch alternation. Secondly, Fig. 2c also showed occasional horizontal lines every 4.5 μm, which occur due to the subfield stitching errors at the EBL patterning. These imply that the product-to-product consistency still has room for improvement, but is expected to be resolved after Xfold Imaging Oy transitions to utilize the low-cost, high-resolution, and high-throughput nanoimprinting fabrication technique.

The AFM scans of the 1L-$MoS_2$ flake in Fig. 2a–c reveal that it nearly completely follows the grating topography due to the capillary and van-der-Waals forces at play. In Fig. 2a, the 3 nm tall and 4 μm wide edge around it is supposed to be $MoO_3$ that has formed due to extended water exposure [36–39] upon transfer and glycerol cleanups. Other flakes also appear to have similar edges, which were observed to be stable, albeit 8 months in air. Interestingly, the $MoO_3$ edge height slightly sloped down by 0–1 nm inwards, which were found to be 4 nm lower than the surrounding grating, thus indicating that the malleable gold grating has deformed by a few nanometers upon transfer.

These AFM images are helpful in the later discussion of the SHG nonuniformity in Fig. 3c–f, which point to imperfections in the $MoS_2$-to-grating adhesion. For instance, some meta-stable suspended 1L-$MoS_2$ is seen as the occasional light-shaded vertical stripes in Fig. 2c. Their meta-stability was observed by subsequent AFM scans, where the former scan in Fig. 2a had visibly 20–30% more

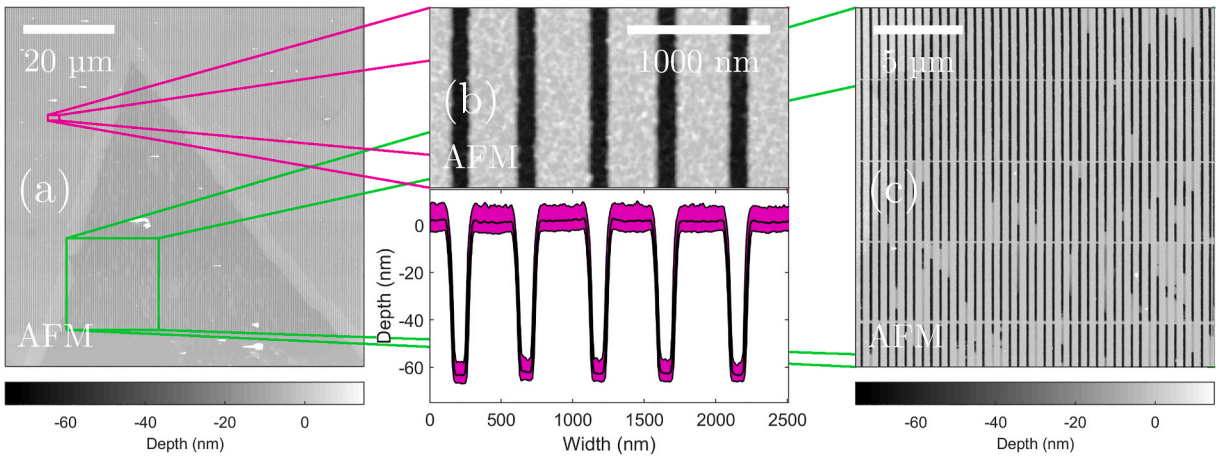


**Fig. 2.** The AFM scans of the Au MG substrate visualizes its grating uniformity and geometry. Image (a) shows an 80 × 80 μm wide grating area, where the 1L-$MoS_2$ flake is visibly surrounded by a 4 μm wide $MoO_3$ oxidation edge. Image (b) shows a close-up view of the surface granularity with 2 nm RMS roughness. Profile (b) is the horizontal cross-section of Image (b), where the purple fill shows the 95% confidence interval and the black line its mean value. This interval translates into 19.4 nm width and 10.6 nm depth variations on average. The grating pitch is 486 nm on average, but exhibits alternating-pitch, where odd and even lines have 466 nm and 506 nm pitches, respectively. Image (c) magnifies into a 20 × 20 μm wide area to better illustrate imperfect adhesion between the flake and the grating, leading to suspended 1L-$MoS_2$ and nonuniform SHG response.

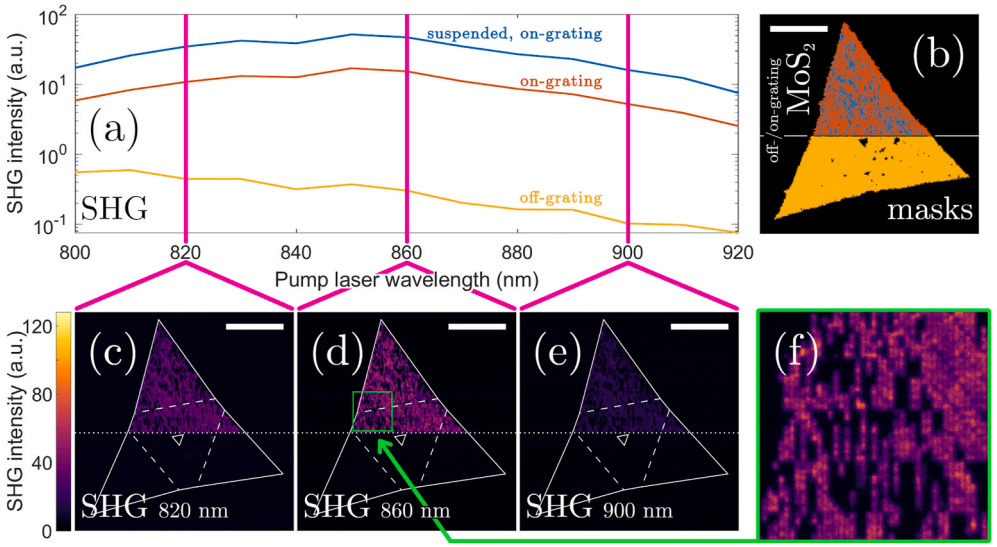


**Fig. 3.** The SHG response of the VLS-grown 1L-$MoS_2$ flake, partially on top of the Au MG substrate pattern. Graph (a) represents the area-averaged SHG intensities on- and off-grating vs. the pump laser wavelength, plotted in log-scale. Image (b) shows the used mask regions to evaluate the corresponding color-coded lines in (a). Images (c), (d), and (e) illustrate the 820, 860, and 900 nm SHG responses, respectively. White lines were added to show the $MoS_2$ layers (solid), the $MoS_2$ grain boundaries (dashed), and the Au grating (dotted). Image (f) magnifies into a 20-by-20 μm wide area at Image (d), which corresponds to the AFM scan in Fig. 2c. White scalebars are 30 μm long.

suspended 1L-$MoS_2$ than that of the latter scan in Fig. 2c. Hence, they are hypothesized to be caused by the trapped pockets of liquid in between the flake and the grating structure. After all, the sample was exposed to KOH solution in one of the steps of the wet-etch transfer [40], where the PMMA/$MoS_2$-layer is detached from the growth substrate and is fished up with the Au MG substrate. Then, PMMA was dissolved by 1 min acetone bath, releasing the flakes at the target substrate, and rinsed by 1 min isopropanol and water baths. Therefore, the trapped liquid is most likely a mixture of these, which could permeate under the relaxing flakes along the grating grooves and through the tiny pores of the evaporated Au walls. The capillary and van-der-Waals forces would then (eventually) make the flakes take their final shapes, locking some pockets of liquid under them.

### 3.2. *On-resonance increase in SHG*

The optical amplification was put to the test by first collecting dozen nonlinear SHG images of the 1L-$MoS_2$ flake at 800–920 nm pump laser wavelengths. The laser spot diameter was approximately 1 μm. Fortunately, this flake has a nonzero rotation angle of 9–10° with respect to the grating direction, allowing it to still generate about 23% of its SHG's six-petal polarization pattern maximum [41,42]. Fig. 3a displays three SHG response curves in log-scale, which were formed by area-averaging each SHG image at the color-coded regions in Fig. 3b. It is immediately evident that the 1L-$MoS_2$ regions on-grating show at least one order of magnitude larger signal than that of the 1L-$MoS_2$ region off-grating, peaking around 850 nm. Three SHG images for 820, 860, and 900 nm in Fig. 3c–e reveal a peculiar nonuniform response, better seen in the magnified 860 nm SHG image in Fig. 3f. The AFM scans in Fig. 2a,c, taken 8 months later, helped to determine that the SHG intensity always peaked in the center of the grating grooves. This was possible after meticulously overlaying data together from every kind of used imaging technique. Fig. S1–S33 in Supplementary Information show the final images prior to their careful comparison for deeper insights. However, due to the inherent diffraction limit, it was not possible to verify if the SHG amplification is strongest near the grating top corners like the simulations [10,17,26] suggest. Additionally, unlike the conformal 1L-$MoS_2$, the suspended 1L-$MoS_2$ was always found to produce an amplified SHG signal. This is explained by the simulations [10,17,26], which show that the suspended monolayer directly intersects the enhanced near-field of the incident light. This and the observed meta-stability of the suspended 1L-$MoS_2$ imply that initially there has been far more suspended 1L-$MoS_2$. Fig. 3f also displays that the SHG amplification is sometimes turned off over the distance of a few grating pitches, which is presumed to be caused by the local adhesion issues of the transferred 1L-$MoS_2$ flakes on the Au grating. Some trapped liquid is believed to locally detach the flake and act as a dielectric screen, impeding the transfer of plasmon-induced hot carriers between 1L-$MoS_2$ and Au observed in direct contact [43–46], which is essential for the electron-hole pair generation. In fact, the transfer of hot carriers between them has been shown to weaken exponentially as a function of distance, halving every 0.99–1.39 nm [43]. The key mechanism behind the turning off is the dielectric screening, which weakens the long-range Coulomb force driving the electron-hole interaction [45,47] that governs the electronic and optical properties of 1L-$MoS_2$ [47]. Interestingly, previous studies have also shown that the SHG intensity of $MoS_2$ is strongly dependent on the electron-hole interaction [48,49] that in turn is highly sensitive to the dielectric screening [43,45,47–49]. For these reasons, the nonuniformity is attributed in general to the dielectric screening due to trapped liquid also causing imperfect $MoS_2$-to-grating adhesion, as inferred previously from Fig. 2a,c.

A more detailed look at the SHG amplification can be taken by dividing all the SHG response curves in Fig. 3a by the 1L-$MoS_2$ off-grating case. The resulting ratios are shown in Fig. 4 (left y-axis) and directly convey the amount of amplification due to the use of the Au MG substrate. The amplification ranges from 30-fold to 170-fold, peaking at 870 nm, and depends strongly on the pump laser wavelength. However, it is important to note that as the SHG of $MoS_2$ has quadratic pump laser power dependence [42], the linear optics amplification would approximately be 5–13-fold or the square root of the SHG's quadratic amplification. Such an increase is possible thanks to the combined effect of the localized SP at the corners and the propagating SP polaritons. Interestingly, when the unpolarized reflectance (right y-axis) is overlaid with the ratio curves, then the amplification maximum matches well with the unpolarized reflectance curve minimum or the SPR dip at 873.7 $\pm$ 1.1 nm, confirming that the amplification has truly occurred due to the use of Au MG substrate. The 2D simulation of slanted MG on a coarse grid had the strongest SPR for the 879 nm cross-polarized 0° plane waves, showing as much as 470,000-fold SHG amplification at the grating top corners. Line averaging resulted in 5,700-fold, 20,000-fold, and 14,000-fold SHG amplifications for the grating top, the suspended 1L-$MoS_2$ at the grating groove, and the conformal 1L-$MoS_2$ at the grating groove, respectively. The conformal case gets its value mostly from the grating slopes because the groove bottom itself only contributes to 29-fold SHG amplification when averaged. In reality, the simulated SHG's quadratic amplifications cannot be reached due to the fabrication imperfections like high surface roughness [50] caused mainly by Au-evaporation. Other influencing factors are EBL patterning of Si-substrate, RIE etching, $O_2$-plasma cleaning, and absorption by 1L-$MoS_2$ (both radiant and nonradiant).

### 3.3. Off-resonance increase in CRM

The 850-nm/glycerol-optimized Au MG substrate was also tested beyond its design, in suboptimal wavelength range and air environment. As the refractive index was changed from 1.47 (glycerol) to 1 (air), the simulated SPR wavelength blueshifted to 619 nm with its dip tail extending down to 560 nm. As the Raman peaks for green laser occur at the 533–534 nm wavelength range, only a minor amplification can be achieved by SP polaritons because the Au absorption impedes their free propagation due to interband transitions.

For the reasons stated above, it was rather surprising to obtain as high as 2–3-fold increase in the Raman peaks so far away from the SPR wavelength in air. These figures exclude the slightly amplified gold fluorescence baseline in the background. Fig. 5a depicts the area-averaged Raman spectra of the 1L-$MoS_2$ flake, which correspond to the colored regions in Fig. 5b. The Raman peaks at 385 $cm^{-1}$ and 404 $cm^{-1}$ in Fig. 5a are the $E^1_{2g}$ and $A_{1g}$ optical phonon modes of 1L-$MoS_2$, respectively. Fig. 5c,d show the $E^1_{2g}$ peak intensity and position, respectively, and Fig. 5e,f show the $A_{1g}$ peak intensity and position, respectively. Correlating these images with those of AFM and SHG reveals that the suspended 1L-$MoS_2$ always resides at the bright spots of Fig. 5c,e. Like in the SHG case, the suspended parts can be more amplified by local fields. As expected, many suspended regions had minor tensile strain with respect to their surroundings, according to Fig. 5d,f using previously reported $-5.2$ $cm^{-1}$/% and $-1.7$ $cm^{-1}$/% conversion ratios [51], respectively. Due to

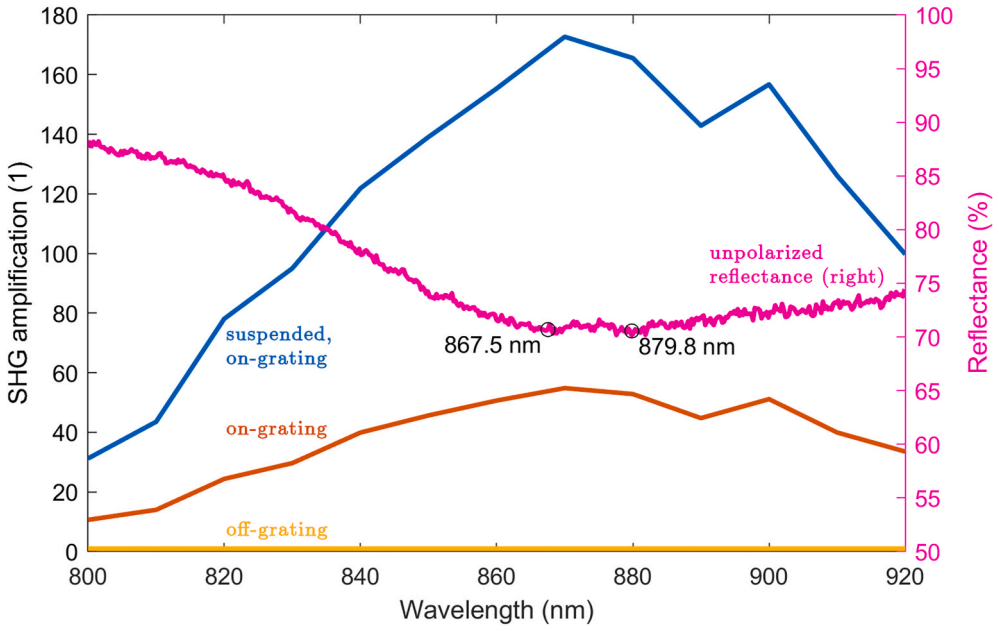


**Fig. 4.** The Au MG substrate SPR wavelength range and its effects are illustrated by the measured SHG amplifications (left y-axis) and the measured unpolarized reflectance (right y-axis). The evaluated amplification curves correspond to the colored regions in Fig. 2b. The SPR dip approximately at 873.7 nm has a fine structure with two local minima at 867.5 and 879.8 nm, which were determined by (not shown) moving geometric mean window size of 20.

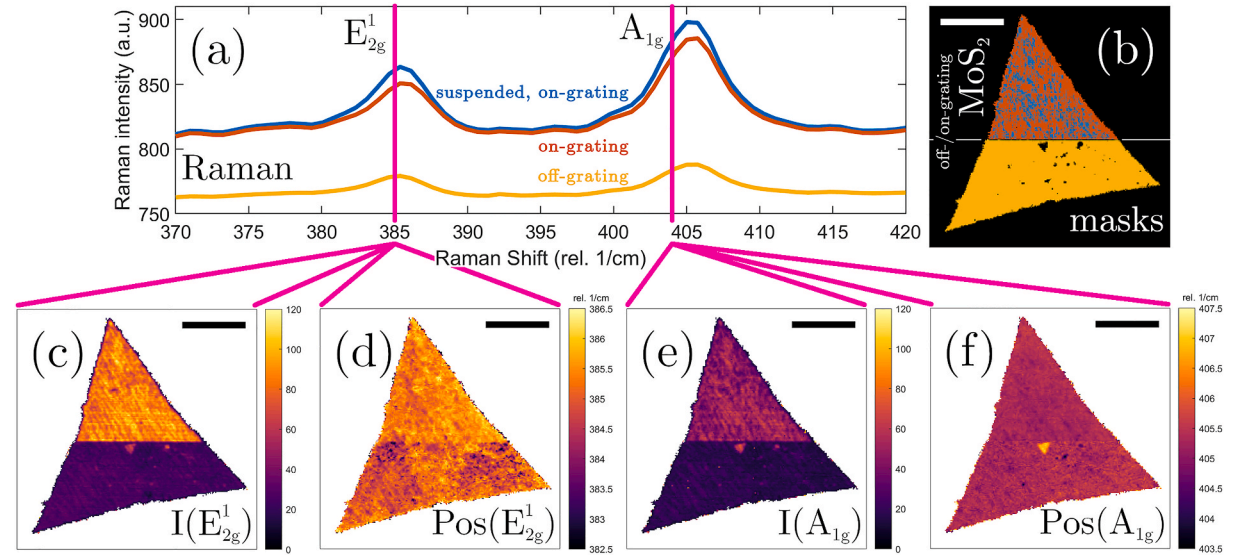


**Fig. 5.** The Raman characterization of the VLS-grown 1L-$MoS_2$ flake, partially on top of the Au MG substrate grating. Graph (a) represents the area-averaged Raman spectra on- and off-grating without baseline subtraction. Image (b) shows the used mask regions to evaluate the corresponding color-coded lines in (a). Images (c), (d), (e) and (f) illustrate the Lorentz-fitted $I(E^1_{2g})$, $Pos(E^1_{2g})$, $I(A_{1g})$, $Pos(A_{1g})$ responses, respectively. Black and white scalebars are 30 μm long.

diffraction-limited low-resolution images, it is difficult to determine why some supposedly suspended regions did not show clear tensile strain, but their strain may be partially relieved by possible underlying trapped liquid. Once again the evidence points towards far more suspended 1L-$MoS_2$ earlier, because of more bright spots in Fig. 3c–f (SHG) and Fig. 5c,e (CRM) than in Fig. 2a,c (AFM).

## 4. Conclusions and future perspectives

This work studied the optical amplification of the VLS-grown 1L-$MoS_2$ on the Au MG substrate in on- and off-resonance cases by two advanced imaging techniques, SHG and CRM, respectively. Interestingly, the hybrid combinations with 2D materials like 1L-$MoS_2$ may spark breakthroughs in optoelectronic devices like photodetectors [24]. The MG substrate with 486 nm grating pitch was geometrically SPR-optimized for a glycerol environment and 850 nm excitation wavelength. It was validated by (simulated and experimental) reflectance and AFM measurements.

The on-resonance case was tested in the 800–920 nm range by the SHG technique in glycerol, where a 170-fold amplification peaked at 870 nm. It was strongest for the suspended 1L-$MoS_2$ and weakest for the collapsed 1L-$MoS_2$ at the bottom of the grating grooves, matching the simulations. However, the simulated values as high as 20,000 did not consider the limiting metal surface roughness [50]. The sample was also purposefully tested in the suboptimal 532 nm off-resonance case by the CRM technique in air, where an unexpected 3-fold amplification was achieved. Hence, it may be worth investigating if these MG substrates can be optimized for a broader wavelength range.

The AFM scans linked the abrupt image nonuniformities to the suspended 1L-$MoS_2$ destabilized by the trapped liquid pockets upon the transfer. The nonuniformity had also degraded over time due to the meta-stable $MoS_2$-to-grating adhesion and is likely linked to the unintentional horizontal barriers every 4.5 μm by the EBL substitching errors. This trapping issue could be mitigated by adding horizontal grooves. Alternatively, the grating grooves could be infilled with solid dielectric material, likely also improving the amplification average and uniformity.

Despite the limitations, these MG substrates can flexibly be tuned to many use cases in the visible or near-infrared range by choosing geometry, metal, and environment. The simple design is quick and easy to tune and test with simulations. Even so, some properties like the polarization sensitivity can be too limiting in some applications. That said, these MG substrates can boost conventional backscattering microscopy due to the reduced laser power, mitigating the photobleaching of biological samples as an example. The manufacturer even claims to use these as nanophotonic biosensors for quick label-free detection of single SARS-CoV-2 viruses [28]. Such a claim is realistic based on the latest rapid developments of the plasmonic-based viral diagnostics [29,30] and is a welcome addition to the joint fight against the upcoming viral threats like the COVID-19 pandemic.

## Declaration of competing interest

The authors declare that they have no known competing financial interests or personal relationships that could have appeared to influence the work reported in this paper.

## Acknowledgement

This work was made possible by the Au MG substrates developed, fabricated, and provided by the Xfold Imaging Oy company. The research was funded by various grants from Aalto University, Finland. Authors acknowledge funding from the Academy of Finland Flagship Programme, Photonics Research and Innovation, decision number: 320167. The experiments were conducted in Aalto University at the OtaNano – Micronova Nanofabrication Centre and in University of Helsinki at the Biomedicum Imaging Unit.

## Appendix A. Supplementary data

Supplementary data to this article can be found online at https://doi.org/10.1016/j.spmi.2021.107077.

## Credit author statement

Joonas Holmi: Conceptualization, Methodology, Software, Validation, Formal analysis, Investigation, Resources, Data Curation, Writing - Original Draft, Writing - Review & Editing, Visualization; Ramesh Raju: Conceptualization, Methodology, Validation, Investigation, Resources, Writing - Original Draft, Writing - Review & Editing, Supervision, Project administration; Jonas Ylönen: Conceptualization, Methodology, Validation, Formal analysis, Investigation, Resources, Writing - Review & Editing; Nagarajan Subramaniyam: Conceptualization, Methodology, Validation, Investigation, Resources, Writing - Review & Editing, Supervision, Project administration, Funding acquisition; Harri Lipsanen: Resources, Writing - Review & Editing, Project administration, Funding acquisition.

## References

[1] E. Ozbay, Plasmonics: merging photonics and electronics at nanoscale dimensions, Science 311 (2006) 189, https://doi.org/10.1126/science.1114849.
[2] R. Zia, J.A. Schuller, A. Chandran, M.L. Brongersma, Plasmonics: the next chip-scale technology, Mater. Today 9 (2006) 20, https://doi.org/10.1016/S1369-7021(06)71572-3.
[3] S. Yan, X. Zhu, J. Dong, Y. Ding, S. Xiao, 2D materials integrated with metallic nanostructures: fundamentals and optoelectronic applications, Nanophotonics 9 (2020) 1877, https://doi.org/10.1515/nanoph-2020-0074.
[4] M.R. Gonçalves, H. Minassian, A. Melikyan, Plasmonic resonators: fundamental properties and applications, J. Phys. D: Appl. Phys. 53 (2020) 443002, https://doi.org/10.1088/1361-6463/ab96e9.
[5] J. Shi, W.-Y. Liang, S.S. Raja, Y. Sang, X.-Q. Zhang, C.-A. Chen, Y. Wang, X. Yang, Y.-H. Lee, H. Ahn, S. Gwo, Plasmonic enhancement and manipulation of optical nonlinearity in monolayer tungsten disulfide, Laser Photonics Rev. 12 (2018) 1800188, https://doi.org/10.1002/lpor.201800188.
[6] P. Genevet, J.P. Tetienne, R. Blanchard, M.A. Kats, J.B. Müller, M.O. Scully, F. Capasso, Enhancement of optical processes in coupled plasmonic nanocavities [Invited], Appl. Opt. 50 (2011) G56, https://doi.org/10.1364/AO.50.000G56.
[7] P. Genevet, J.P. Tetienne, E. Gatzogiannis, R. Blanchard, M.A. Kats, M.O. Scully, F. Capasso, Large enhancement of nonlinear optical phenomena by plasmonic nanocavity gratings, Nano Lett. 10 (2010) 4880, https://doi.org/10.1021/nl102747v.
[8] A.K. Agrawal, A. Ninawe, A. Dhawan, Non-uniform narrow groove plasmonic nano-gratings for SPR sensing and imaging, IEEE Access 9 (2021) 10136, https://doi.org/10.1109/ACCESS.2021.3050201.
[9] C. Niu, T. Huang, X. Zhang, H. Liu, W. Zhang, J. Hu, Surface plasmon-enhanced optical absorption in monolayer $MoS_2$ with one-dimensional Au grating, Plasmonics 10 (2015) 419, https://doi.org/10.1007/s11468-014-9823-z.
[10] J. Song, L. Lu, Q. Cheng, Z. Luo, Surface plasmon-enhanced optical absorption in monolayer $MoS_2$ with one-dimensional Au grating, J. Quant. Spectrosc. Radiat. Transf. 211 (2018) 138, https://doi.org/10.1016/j.jqsrt.2018.02.036.
[11] C.M. Galloway, C. Artur, J. Grand, E.C. Le Ru, Photobleaching of fluorophores on the surface of nanoantennas, J. Phys. Chem. C 118 (2014) 28820, https://doi.org/10.1021/jp510105z.
[12] X. Fan, Q. Hao, T. Qiu, P.K. Chu, Improving the performance of light-emitting diodes via plasmonic-based strategies, J. Appl. Phys. 127 (2020), 040901, https://doi.org/10.1063/1.5129365.
[13] Y.C. Chang, B.H. Huang, T.H. Lin, Surface-enhanced Raman scattering and fluorescence on gold nanogratings, Nanomaterials 10 (2020) 776, https://doi.org/10.3390/nano10040776.
[14] M. Bauch, K. Toma, M. Toma, Q. Zhang, J. Dostalek, Plasmon-enhanced fluorescence biosensors: a review, Plasmonics 9 (2014) 781, https://doi.org/10.1007/s11468-013-9660-5.
[15] S.H. Kim, S.S. Oh, K.J. Kim, J.E. Kim, H.Y. Park, O. Hess, C.S. Kee, Localized surface plasmon resonance spectroscopy and sensing, Annu. Rev. Phys. Chem. 58 (2007) 267, https://doi.org/10.1146/annurev.physchem.58.032806.104607.
[16] H. Aouani, O. Mahboub, E. Devaux, H. Rigneault, T.W. Ebbesen, J. Wenger, Plasmonic antennas for directional sorting of fluorescence emission, Nano Lett. 11 (2011) 2400, https://doi.org/10.1021/nl200772d.
[17] J. Ylönen, Simulation of resonant nanostructures for electric near field enhancement, M.Sc. thesis,, Aalto University School of Electrical Engineering, 2018, http://urn.fi/URN:NBN:fi:aalto-201802231645.
[18] M.L. Noordam, J. Hernandez-Rueda, L.Y. Talsma, L. Kuipers, Plasmon-induced enhancement of nonlinear optical processes in a double-resonant metallic nanostructure grating, Appl. Phys. Lett. 116 (2020) 101101, https://doi.org/10.1063/1.5141408.
[19] Z. Wang, Z. Dong, H. Zhu, L. Jin, M.-H. Chiu, L.-J. Li, Q.-H. Xu, G. Eda, S.A. Maier, A.T.S. Wee, et al., Selectively plasmon-enhanced second-harmonic generation from monolayer tungsten diselenide on flexible substrates, ACS Nano 12 (2018) 1859, https://doi.org/10.1021/acsnano.7b08682.
[20] A.C. Ferrari, F. Bonaccorso, V. Fal'ko, K.S. Novoselov, S. Roche, P. Bøggild, S. Borini, F.H.L. Koppens, V. Palermo, N. Pugno, et al., Science and technology roadmap for graphene, related two-dimensional crystals, and hybrid systems, Nanoscale 7 (2015) 4598, https://doi.org/10.1039/C4NR01600A.
[21] J. Shim, H.-Y. Park, D.-H. Kang, J.-O. Kim, S.-H. Jo, Y. Park, J.-H. Park, Electronic and optoelectronic devices based on two-dimensional materials: from fabrication to application, Adv. Electron. Mater. 3 (2017) 1600364, https://doi.org/10.1002/aelm.201600364.
[22] X. Li, L. Tao, Z. Chen, H. Fang, X. Li, X. Wang, J.-B. Xu, H. Zhu, Graphene and related two-dimensional materials: structure-property relationships for electronics and optoelectronics, Appl. Phys. Rev. 4 (2017), 021306, https://doi.org/10.1063/1.4983646.
[23] Z. Sun, A. Martinez, F. Wang, Optical modulators with 2D layered materials, Nat. Photonics 10 (2016) 227, https://doi.org/10.1038/nphoton.2016.15.
[24] Y. Li, Z. Li, C. Chi, H. Shan, L. Zheng, Z. Fang, Plasmonics of 2D nanomaterials: properties and applications, Adv. Sci. 4 (2017) 1600430, https://doi.org/10.1002/advs.201600430.

[25] Y. Yang, W.G. Liu, Z.T. Lin, R.H. Pan, C.Z. Gu, J.J. Li, Plasmonic hybrids of two-dimensional transition metal dichalcogenides and nanoscale metals: architectures, enhanced optical properties and devices, Mater. Today Phys. 17 (2021) 100343, https://doi.org/10.1016/j.mtphys.2021.100343.
[26] S. Kwon, S.-Y. Lee, S.H. Choi, J.-W. Kang, T. Lee, J. Song, S.W. Lee, C.-H. Cho, K.K. Kim, K.-J. Yee, D.-W. Kim, Polarization-dependent light emission and charge creation in $MoS_2$ monolayers on plasmonic Au nanogratings, ACS Appl. Mater. Interfaces 12 (2020) 44088, https://doi.org/10.1021/acsami.0c13436.
[27] Y. Zhou, G. Scuri, D.S. Wild, A.A. High, A. Dibos, L.A. Jauregui, C. Shu, K. De Greve, K. Pistunova, A.Y. Joe, et al., Probing dark excitons in atomically thin semiconductors via near-field coupling to surface plasmon polaritons, Nat. Nanotechnol. 12 (2017) 856, https://doi.org/10.1038/nnano.2017.106.
[28] Xfold Imaging Oy, the glass- and silicon-based metal grating substrates and their biological imaging applications. https://www.xfoldimaging.com. (Accessed 12 August 2021).
[29] A.M. Shrivastav, U. Cvelbar, I. Abdulhalim, A comprehensive review on plasmonic-based biosensors used in viral diagnostics, Commun. Biol. 4 (2021) 1, https://doi.org/10.1038/s42003-020-01615-8.
[30] M. Soler, M.C. Estevez, M. Cardenosa-Rubio, A. Astua, L.M. Lechuga, How nanophotonic label-free biosensors can contribute to rapid and massive diagnostics of respiratory virus infections: COVID-19 case, ACS Sens. 5 (2020) 2663, https://doi.org/10.1021/acssensors.0c01180.
[31] X. Bai, S. Li, S. Das, L. Du, Y. Dai, L. Yao, R. Raju, M. Du, H. Lipsanen, Z. Sun, Single-step chemical vapour deposition of anti-pyramid $MoS_2/WS_2$ vertical heterostructures, Nanoscale 11 (2021) 4537, https://doi.org/10.1039/D0NR08281C.
[32] S. Li, Y.-C. Lin, X.-Y. Liu, Z. Hu, J. Wu, H. Nakajima, S. Liu, T. Okazaki, W. Chen, T. Minari, et al., Wafer-scale and deterministic patterned growth of monolayer $MoS_2$ via vapor–liquid–solid method, Nanoscale 11 (2019) 16122, https://doi.org/10.1039/C9NR04612G.
[33] H. Kim, Y.-G. Yoon, H. Ko, S.M. Kim, H. Rho, Charge transfer across monolayer/bilayer $MoS_2$ lateral interface and its influence on exciton and trion characteristics, 2D Mater. 6 (2019), 025004, https://doi.org/10.1088/2053-1583/aafa52.
[34] N. Subramaniyam, M. Sopanen, E. Ikonen, A. Isomäki, S. Pfisterer, A Plasmonic device, U.S. Patent No. 2019/0391302 A1, 2019. https://patents.google.com/patent/US20190391302A1/en.
[35] J.T. Holmi, WITio: a MATLAB toolbox for WITec Project/Data (*.wip/*.wid) files (Version 2.0.0), GitLab repository, February 11, 2021. https://gitlab.com/jtholmi/wit_io.
[36] T.Y. Ko, A. Jeong, W. Kim, J. Lee, Y. Kim, J.E. Lee, G.H. Ryu, K. Park, D. Kim, Z. Lee, et al., On-stack two-dimensional conversion of $MoS_2$ into $MoO_3$, 2D Mater. 4 (2016), 014003, https://doi.org/10.1088/2053-1583/4/1/014003.
[37] J. Li, S. Hu, S. Wang, H. Kang, Z. Chen, S. Zhao, Y. Zhang, Y. Sui, G. Yu, The degradation of CVD-grown $MoS_2$ domains in atmospheric environment, Mater. Lett. 290 (2021) 129421, https://doi.org/10.1016/j.matlet.2021.129421.
[38] J.C. Kotsakidis, Q. Zhang, A.L. Vazquez de Parga, M. Currie, K. Helmerson, D.K. Gaskill, M.S. Fuhrer, Oxidation of monolayer $WS_2$ in ambient is a photoinduced process, Nano Lett. 19 (2019) 5205, https://doi.org/10.1021/acs.nanolett.9b01599.
[39] X. Zhang, F. Jia, B. Yang, S. Song, Oxidation of molybdenum disulfide sheet in water under in situ atomic force microscopy observation, J. Phys. Chem. C 121 (2017) 9938, https://doi.org/10.1021/acs.jpcc.7b01863.
[40] H. Kwon, P.J. Jeon, J.S. Kim, T.-Y. Kim, H. Yun, S.W. Lee, T. Lee, S. Im, Large scale $MoS_2$ nanosheet logic circuits integrated by photolithography on glass, 2D Mater. 3 (2016), 044001, https://doi.org/10.1088/2053-1583/3/4/044001.
[41] W.-T. Hsu, Z.-A. Zhao, L.-J. Li, C.-H. Chen, M.-H. Chiu, P.-S. Chang, Y.-C. Chou, W.-H. Chang, Second harmonic generation from artificially stacked transition metal dichalcogenide bilayers, ACS Nano 8 (2014) 2951, https://doi.org/10.1021/nn500228r.
[42] L. Mennela, M. Paur, T. Muellera, Second harmonic generation in strained transition metal dichalcogenide monolayers: $MoS_2$, $MoSe_2$, $WS_2$, and $WSe_2$, APL Photonics 4 (2019), 034404, https://doi.org/10.1063/1.5051965.
[43] C. Xu, H.W. Yong, J. He, R. Long, A.R. Cadore, I. Paradisanos, A.K. Ott, G. Soavi, S. Tongay, G. Cerullo, A.C. Ferrari, et al., Weak distance dependence of hot-electron-transfer rates at the interface between monolayer $MoS_2$ and gold, ACS Nano 15 (2020) 819, https://doi.org/10.1021/acsnano.0c07350.
[44] I. Irfan, S. Golovynskyi, M. Bosi, L. Seravalli, O.A. Yeshchenko, B. Xue, D. Dong, Y. Lin, R. Qiu, B. Li, J. Qu, Enhancement of Raman scattering and exciton/trion photoluminescence of monolayer and few-layer $MoS_2$ by Ag nanoprisms and nanoparticles: shape and size effects, J. Phys. Chem. C 125 (2021) 4119, https://doi.org/10.1021/acs.jpcc.0c11421.
[45] M. Wang, W. Li, L. Scarabelli, B.B. Rajeeva, M. Terrones, L.M. Liz-Marzán, D. Akinwande, Y. Zheng, Plasmon–trion and plasmon–exciton resonance energy transfer from a single plasmonic nanoparticle to monolayer $MoS_2$, Nanoscale 9 (2017) 13947, https://doi.org/10.1039/C7NR03909C.
[46] S. Kwon, M.H. Kwon, J. Song, E. Kim, Y. Kim, B.R. Kim, J.K. Hyun, S.W. Lee, D.-W. Kim, Light-induced surface potential modification in MoS2 monolayers on Au nanostripe arrays, Sci. Rep. 9 (2019) 1, https://doi.org/10.1038/s41598-019-50950-2.
[47] M.D. Tran, J.-H. Kim, Y.H. Lee, Tailoring photoluminescence of monolayer transition metal dichalcogenides, Curr. Appl. Phys. 16 (2016) 1159, https://doi.org/10.1016/j.cap.2016.03.023.
[48] M. Grüning, C. Attaccalite, Second harmonic generation in h-BN and $MoS_2$ monolayers: role of electron-hole interaction, Phys. Rev. B 89 (2014), 081102, https://doi.org/10.1103/PhysRevB.89.081102.
[49] X. Wen, W. Xu, W. Zhao, J.B. Khurgin, Q. Xiong, Plasmonic hot carriers-controlled second harmonic generation in $WSe_2$ bilayers, Nano Lett. 18 (2018) 1686, https://doi.org/10.1021/acs.nanolett.7b04707.
[50] E.J.O.C. Kretschmann, The angular dependence and the polarisation of light emitted by surface plasmons on metals due to roughness, Opt. Commun. 5 (1972) 331, https://doi.org/10.1016/0030-4018(72)90026-0.
[51] D. Lloyd, X. Liu, J.W. Christopher, L. Cantley, A. Wadehra, B.L. Kim, B.B. Goldberg, A.K. Swan, J.S. Bunch, Band gap engineering with ultralarge biaxial strains in suspended monolayer $MoS_2$, Nano Lett. 16 (2016) 5836, https://doi.org/10.1021/acs.nanolett.6b02615.